Check for updates

JGR Oceans

RESEARCH ARTICLE
10.1029/2023JC019964

Key Points:

- Seismic and ADCP data reveal 11 mesoscale eddies, mostly intra-halocline anticyclones, in the western Arctic Ocean
- Diffusivities at the edges of these eddies were generally enhanced and can be up to 10^{-4} m^2 s^{-1}
- Enhanced diffusivities are attributed to shear instabilities and submesoscale motions

Correspondence to:

H. Song,
hbsong@tongji.edu.cn

Citation:

Yang, S., Song, H., Coakley, B., & Zhang, K. (2023). Enhanced mixing at the edges of mesoscale eddies observed from high-resolution seismic data in the western Arctic Ocean. *Journal of Geophysical Research: Oceans*, *128*, e2023JC019964. https://doi.org/10.1029/2023JC019964

Received 21 APR 2023
Accepted 25 SEP 2023

© 2023. American Geophysical Union. All Rights Reserved.

Enhanced Mixing at the Edges of Mesoscale Eddies Observed From High-Resolution Seismic Data in the Western Arctic Ocean

Shun Yang[1,2], Haibin Song[1,2], Bernard Coakley[3], and Kun Zhang[1,2]

[1]School of Ocean and Earth Science, Tongji University, Shanghai, China, [2]State Key Laboratory of Marine Geology, Tongji University, Shanghai, China, [3]Geophysical Institute, University of Alaska Fairbanks, Fairbanks, AK, USA

Abstract In recent years, the Arctic Ocean has experienced a dramatic decrease in sea ice cover, leading to enhanced turbulent mixing and eddy activity. Due to the scarcity of high-resolution observations, our understanding of turbulent mixing in the Arctic is incomplete. Using three seismic reflection transects with high spatial resolution ($\sim O$ (10) m) and concurrent ADCP-derived current velocity, this study identified 11 mesoscale eddies on the ice-free Chukchi Borderlands of the western Arctic Ocean. 82% of them are intra-halocline anticyclones. The total length of horizontal scales of these 11 eddies occupies ~40% of the total length of three seismic lines. Diapycnal diffusivities estimated from seismic data were enhanced and can be up to 10^{-4} m^2 s^{-1} at the edges of these eddies, compared with the average values ($\sim 10^{-6}$ m^2 s^{-1}) at the Chukchi Borderlands. Seismic-estimated diffusivities were validated by fine-scale parameterization using ADCP-derived velocity data and historical hydrographic data. Enhanced diffusivities at the edges of eddies may be attributed to shear instabilities at the top and bottom edges and to submesoscale motions at the lateral edges of these eddies. We highlight the enhanced mixing at the edges of eddies in the halocline can increase the upward heat flux. This upward heat flux can transfer the heat of the warm Atlantic water below to the surface, which may further promote the melting of surface sea ice.

Plain Language Summary Turbulence is widely present in the ocean and is crucial for maintaining ocean mixing. In the past, due to sea ice cover, the Arctic Ocean was considered a region of weak turbulent mixing. However, in recent years, the sea ice in the Arctic Ocean has gradually decreased, and the Arctic Ocean is becoming more active. However, due to the lack of high-resolution observations, our understanding of turbulent mixing in the Arctic Ocean is still insufficient. This paper uses the high-resolution seismic reflection method, a traditional method in oil exploration, to estimate the turbulent mixing intensity in the western Arctic Ocean. The results indicate that the mixing rate at the edges of the eddies in the halocline is much higher than the background value. The enhanced mixing at the edges of eddies in the halocline can increase the upward heat flux. This upward heat flux can transfer the heat of the warm Atlantic water below to the surface, which may further promote the melting of surface sea ice.

1. Introduction

The ocean overturning circulation plays a major role in the climate system by its role in controlling the exchange of heat and carbon in the ocean (Hansen et al., 1985). Ocean overturning circulation is maintained by turbulent mixing (Mashayek et al., 2017; Munk & Wunsch, 1998); without deep mixing, the ocean would turn into a stagnant pool of cold salty water within a few thousand years (Munk & Wunsch, 1998). Turbulent mixing is an important energy source of large-scale ocean dynamics, from which energy is transferred progressively down-scale to smaller scales that are subjected to dissipation and mixing processes (Whalen et al., 2018). Moreover, a key element of ocean models is the parameterization of the relationship between turbulent mixing and internal wave energy (Wunsch & Ferrari, 2004). Studying turbulent mixing can not only improve our understanding of the physical processes involved in the interactions between multiscale motions but also enhance the accuracy of ocean models for climate simulation and prediction.

The Arctic Ocean has been considered a region of weak turbulent mixing due to its long-term ice cover (Rainville & Winsor, 2008). Moreover, the Arctic Ocean has a strong halocline, with weak mixing, which is essential in isolating the main oceanic heat source (i.e., the warm Atlantic Water at intermediate depths) from the surface and the sea ice (e.g., Carmack et al., 2015; Fer, 2009). The Canada Basin halocline is located above 250 m depth,

21699291, 2023, 10, Downloaded from https://agupubs.onlinelibrary.wiley.com/doi/10.1029/2023JC019964 by Tongji University, Wiley Online Library on [05/09/2024]. See the Terms and Conditions (https://onlinelibrary.wiley.com/terms-and-conditions) on Wiley Online Library for rules of use; OA articles are governed by the applicable Creative Commons License

where salinity increases rapidly with depth, and temperature is close to freezing. Below the halocline is warm and salty North Atlantic water, located at about 250–800 m (Timmermans et al., 2008). In the past few decades, however, reducing seasonal ice cover has led to an increased coupling between the atmosphere and the ocean. As a result, the turbulent mixing in the Arctic Ocean may have intensified (Nghiem et al., 2007; Rippeth & Fine, 2022).

Less sea ice enables more energetic ocean movements, which not only enhances turbulent mixing but also promotes the generation and development of mesoscale eddies (Rippeth & Fine, 2022). The Beaufort Gyre and Chukchi Slope Current regions are active eddy areas (Zhao et al., 2016), spawning new eddies annually. In fact, there are a large number of mesoscale and submesoscale eddies in and around the Canada Basin (e.g., Carpenter & Timmermans, 2012; Manley & Hunkins, 1985; Muench et al., 2000; Spall et al., 2008; Timmermans et al., 2008; Zhao et al., 2014, 2016; Zhao & Timmermans, 2015). For example, Manley and Hunkins (1985) estimated that mesoscale eddies occupy at least 25% of the sea surface area of the Beaufort Sea. Most of the intra-halocline eddies in the Canada Basin are anticyclonic eddies, and cold eddies dominate (Zhao et al., 2014, 2016). The eddies are concentrated on the west and south sides of the basin, which is close to the topographic edge and the boundary of the Beaufort Gyre (Zhao et al., 2016).

Then the question is, do the eddies in the Arctic halocline enhance the vertical heat exchange? If the answer is yes, the transfer of the intermediate-depth heat (the warm Atlantic Water) to the surface, and thus its role in sea ice melting, can be facilitated by vertical exchange processes. In most regions of the global ocean, the vertical exchange is mainly controlled by turbulent stirring, which increases the mixing rate by many orders of magnitude compared to molecular diffusion (Rippeth & Fine, 2022). Due to the lack of sufficient observations with high resolution, our knowledge of the turbulent mixing of intra-halocline eddies in the Arctic Ocean is still inadequate.

Seismic reflection images of the seawater columns can be used to estimate the turbulent mixing. This method has a much higher horizontal resolution, $\sim O$ (10) m, than traditional oceanographic observations (Holbrook et al., 2003). Holbrook and Fer (2005) first showed that the horizontal wavenumber spectrum, of fluctuations of seismic reflectors, conforms to the Garrett-Munk internal wave spectrum (Garrett & Munk, 1975). Subsequently, Klymak and Moum (2007a, 2007b) confirmed this conjecture using the isopycnal slope spectrum of horizontal tow observations. Their results showed that the characteristics of turbulence can extend to the astonishing horizontal wavelength of hundreds of meters, which is within the wavelength range that seismic data can distinguish. Sheen et al. (2009) applied the slope spectrum method of Klymak and Moum (2007a, 2007b) to seismic images for the first time, obtaining the spatial distribution of diapycnal diffusivity on the Southern Ocean seismic transect. Holbrook et al. (2013) explained the details of the process of estimating turbulent dissipation using seismic data and discussed the factors affecting the dissipation estimation. This method was widely used to estimate the turbulent mixing of various ocean phenomena or regions, such as Mediterranean eddies (Bai et al., 2015; Xiao & Meng, 2022) and the Gulf of Alaska eddies (Tang et al., 2020), internal solitary waves (Gong et al., 2021) and internal waves (Bai et al., 2015; Dickinson et al., 2017; Fortin et al., 2016), above seamounts and ridges (Tang et al., 2021, 2022; Wei et al., 2022), and front regions (Gunn et al., 2021).

This study further investigates eddies in the western Arctic Ocean based on S. Yang et al. (2022) and K. Zhang et al. (2022). Using the seismic reflection data and ADCP-derived velocity data collected simultaneously in September 2011, we observed intra-halocline eddies and the Atlantic Water eddies on the ice-free Chukchi Borderlands. We then estimated the distribution of diapycnal diffusivities using the seismic reflection data, which are validated by hydrographic data using fine-scale parameterization.

2. Data and Methods

2.1. Seismic Acquisition and Processing

Multi-channel seismic reflection data was acquired by the R/V Marcus G. Langseth in the northern Chukchi Sea, Arctic Ocean, during the MGL1112 cruise in September 2011 (Coakley, 2014). This paper uses three seismic lines: 03BA, 04, and 07B (Figure 1). The acquisition dates of the three lines are September 19-21, 21–22, and 26–27, respectively (Table 1). The acquisition vessel towed an 1,830 in^3 (30 L) combined airgun array, which fired every 37.5 m (i.e., shot spacing). The reflected signal was received by 468 seismic channels on a 5,850 m long towed streamer after reflection through the water column. The receiver channel spacing is 12.5 m. The distances from the source to the nearest receiver (i.e., the minimum offset) is 226.7 m for lines 03BA and 04, and

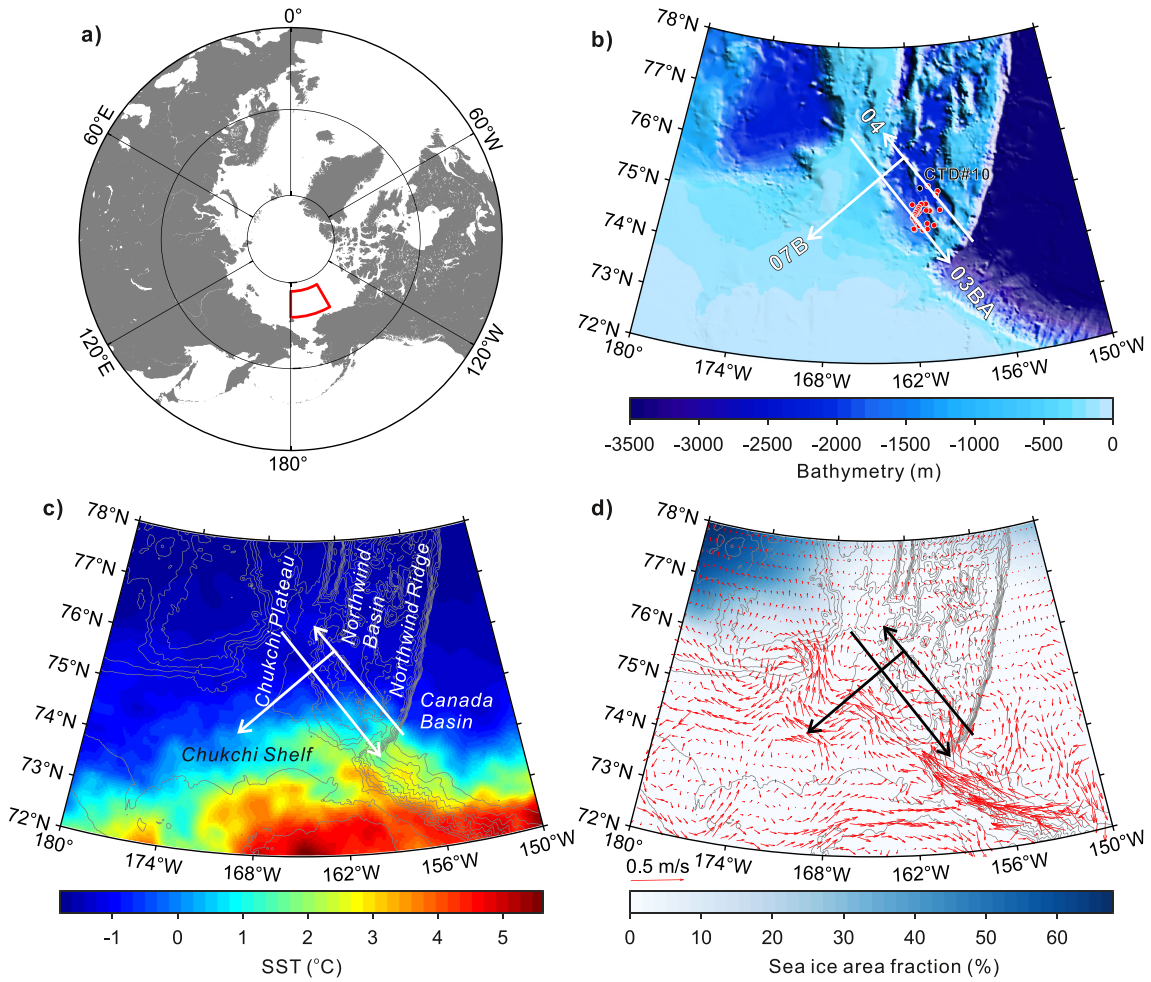

Figure 1. Location map of seismic lines. (a) Location of the study region (red box). (b) Bathymetric map of the study region. Three white long arrows are seismic lines 03BA, 04, and 07B. Red dots are historical CTD (conductivity, temperature, and depth) stations. The black dot is CTD No.10. (c) Monthly average Sea surface temperature (SST) from multi-satellite observations with a center date of 20 September 2011, with a processing level L4 and a spatial resolution of 5 km (available from NERC Earth Observation Data Acquisition and Analysis Service (NEODAAS) and at https://data.neodaas.ac.uk/visualisation/). Gray contours are isobaths. (d) The color map is the monthly average sea ice area fraction based on multi-satellite observations at the date centered 21 September 2011 (available from NERC Earth Observation Data Acquisition and Analysis Service (NEODAAS) and at https://data.neodaas.ac.uk/visualisation/). Red arrows are sea surface geostrophic currents based on multi-satellite observations on 21 September 2011, with a processing level of L4 and spatial resolution of 0.25° (available from Copernicus Marine Environment Monitoring Service (CMEMS) and at https://data.marine.copernicus.eu/product/SEALEVEL_GLO_PHY_L4_MY_008_047/description). Gray contours are isobaths. Three long black arrows are seismic lines.

206.7 m for line 07B, respectively. The time interval of each channel record is 2 ms. During seismic acquisition, the ship speed was about 3 m s^{-1}.

The seismic processing flow used here is similar to that employed by S. Yang et al. (2022). The steps include (a) defining the geometry, (b) suppressing direct waves and de-noising, (c) velocity analysis, (d) normal move-out correction, (e) stacking, (f) time migration, and (g) de-noising. The specific processing steps are not repeated here, but a few points still need to be emphasized. Holbrook et al. (2013) summarized several issues that require attention when doing spectral analysis on seismic reflection data, especially the need to suppress random and harmonic noise. To improve the signal-to-noise ratio (*S*/*N*) of the seismic data, we performed band-pass filtering in the frequency domain and dip filtering in the F-K (frequency-wavenumber) domain (Yilmaz, 2001) after stacking. The frequency combination of the trapezoidal window used for frequency domain band-pass filtering here is 8-12-100-110 Hz. We found that there is strong vertical noise in seismic transects, which may be caused

Table 1
Seismic Acquisition Information

Line	Date	Length (km)	Azimuth
03BA	19–21/09/2011	338.8	NW-SE
04	21–22/09/2011	298.5	SE-NW
07B	26–27/09/2011	271.0	NE-SW

21699291, 2023, 10, Downloaded from https://agupubs.onlinelibrary.wiley.com/doi/10.1029/2023JC019964 by Tongji University, Wiley Online Library on [05/09/2024]. See the Terms and Conditions (https://onlinelibrary.wiley.com/terms-and-conditions) on Wiley Online Library for rules of use; OA articles are governed by the applicable Creative Commons License

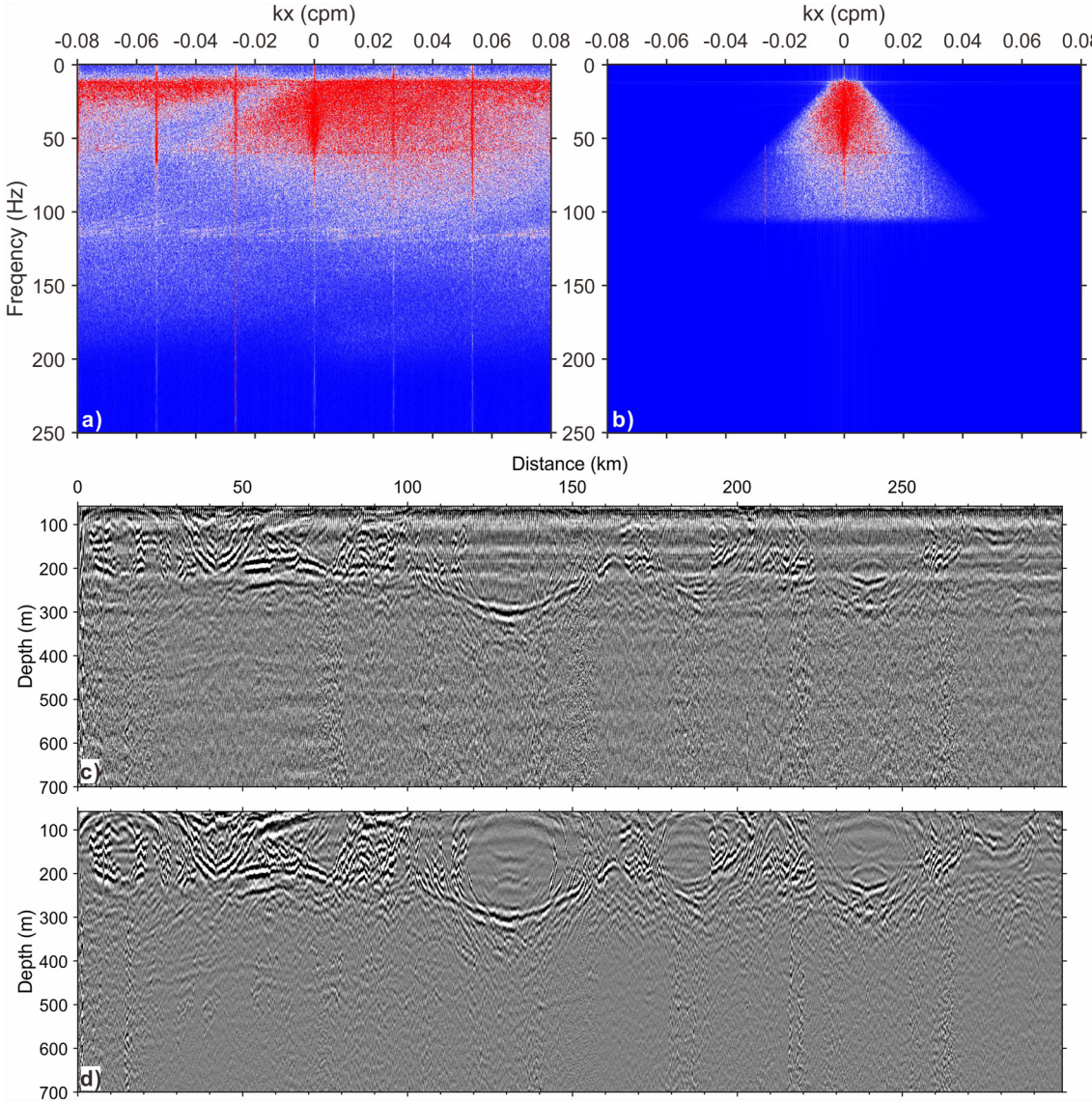

Figure 2. Seismic image of line 04 and its F-K spectrum. (a) and (b) are the F-K spectra of before and after F-K filtering and bandpass filtering, respectively. (c) and (d) are the seismic images before and after F-K filtering and bandpass filtering, respectively.

by swell. F-K domain dip filtering (the slope in the F-K domain is equal to the reciprocal of the slope in the distance-time domain) can effectively suppress the noise caused by the swell (Figure 2).

Figure 2 shows clear harmonic noise in the horizontal wavenumber domain. The wave numbers of these noise peaks are related to the shot spacing (Holbrook et al., 2013), respectively 1/37.5, 2/37.5, and 3/37.5 cpm. Notch filtering can effectively remove the harmonic noise (see Section 2.3), and also improve the continuity of seismic reflectors so that more reflectors can be picked (Tang et al., 2021).

The subsequent spectral analysis requires a high *S*/*N* for the seismic data. According to Holbrook et al. (2013), the *S*/*N* of any two adjacent traces in the seismic data is

$$\frac{S}{N} = \sqrt{\frac{|c|}{|a-c|}}, \tag{1}$$

where c is the maximum value of the cross-correlation of the two adjacent traces, and a is the zero-lag autocorrelation value of the first trace. To calculate the *S*/*N* of a segment of data, we use Equation 1 to calculate the *S*/*N*

21699291, 2023, 10, Downloaded from https://agupubs.onlinelibrary.wiley.com/doi/10.1029/2023JC019964 by Tongji University, Wiley Online Library on [05/09/2024]. See the Terms and Conditions (https://onlinelibrary.wiley.com/terms-and-conditions) on Wiley Online Library for rules of use; OA articles are governed by the applicable Creative Commons License

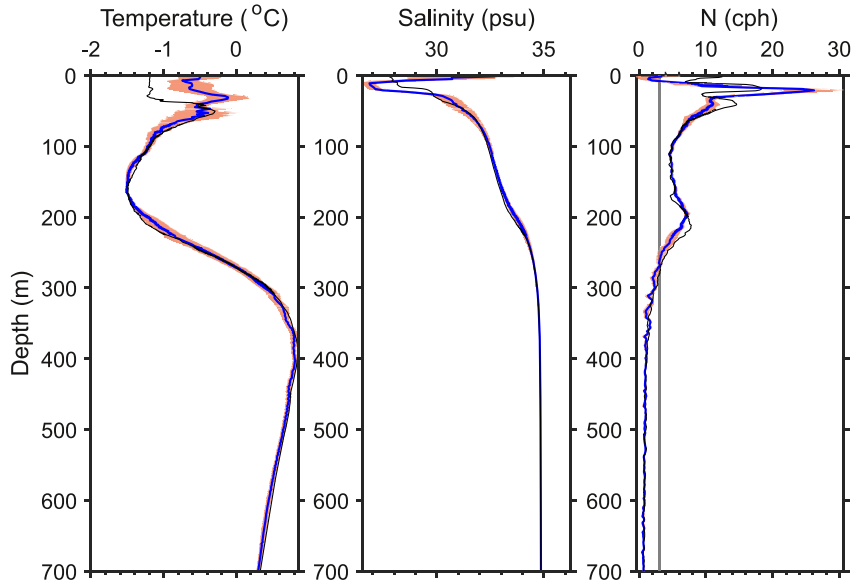

Figure 3. The mean values (blue curves) and their 95% confidence intervals (red shade) of temperature, salinity, and buoyancy frequency (N) derived from CTD casts in Figure 1b for the same period (September) in the region. The thin black curves are the values of CTD No.10 in Figure 1b. The gray line in the right panel is the reference buoyancy frequency $N_0 = 3$ cph.

value of each pair of adjacent traces, and then calculate the median *S*/*N* of the segment. The median *S*/*N* values of the three transects 03BA, 04, and 07B are 10.99, 9.67, and 12.39, respectively, much greater than 4, which meets the requirement for spectral analysis (e.g., Holbrook et al., 2013).

It should be noted that only the nearest 100 traces of the original 468 receivers were used for stacking. Unlike solid strata, seawater is constantly moving. Therefore, a long receiving length, for the same middle point, means an increased acquisition time across a gather, which will cause the water column reflections at different times of the same middle point to be stacked, resulting in a "temporal blurring" effect (Falder et al., 2016). Using fewer traces in each gather, will reduce the *S*/*N* but reduce the "temporal blurring" effect.

2.2. Hydrographic Data

2.2.1. Velocity Data Derived From Concurrent ADCP

A shipboard acoustic Doppler current profiler (ADCP) was also used to carry out horizontal current velocity measurements simultaneously with the seismic acquisition. The current velocity was collected using the UHDAS system and processed using the CODAS software (https://currents.soest.hawaii.edu/docs/adcp_doc/index.html), both of which were developed and maintained by University of Hawaii (Firing et al., 2012). The observed velocity components in the latitudinal and longitudinal directions are u and v, respectively, which can be composed into the total horizontal velocity $\boldsymbol{U}$. We can calculate the normal flow velocity of the seismic transect, $U_n = u\cos\theta - v\sin\theta$, where θ is the azimuth angle of the vessel. The time sampling interval was 300 s. The vessel's sailing speed was about 3 m s^{-1} during acquisition, so the horizontal sampling interval of the velocity is about 0.9 km. Vertically, the data is divided into 60 layers, each representing an average of 16 m, so the depth range is 31–975 m.

2.2.2. Temperature and Salinity Derived From Historical CTDs

A key parameter for estimating the mixing parameters is the local buoyancy frequency. Since there are no in situ temperature and salinity data, we cannot obtain the real-time local buoyancy frequency. Here we use the historical temperature and salinity data observed from 47 CTD casts (Figure 1b) around the seismic lines in the same month (September), to obtain the background buoyancy frequency $N(z) = \sqrt{-\frac{g\partial\rho}{\rho\partial z}}$, where g is the gravitational acceleration, and ρ is the density (Figure 3).

21699291, 2023, 10, Downloaded from https://agupubs.onlinelibrary.wiley.com/doi/10.1029/2023JC019964 by Tongji University, Wiley Online Library on [05/09/2024]. See the Terms and Conditions (https://onlinelibrary.wiley.com/terms-and-conditions) on Wiley Online Library for rules of use; OA articles are governed by the applicable Creative Commons License

21699291, 2023, 10, Downloaded from https://agupubs.onlinelibrary.wiley.com/doi/10.1029/2023JC019964 by Tongji University, Wiley Online Library on [05/09/2024]. See the Terms and Conditions (https://onlinelibrary.wiley.com/terms-and-conditions) on Wiley Online Library for rules of use; OA articles are governed by the applicable Creative Commons License

2.3. Estimating Diffusivity Using Seismic Data

Estimating diapycnal diffusivity from seismic images can be from not only the turbulent regime (e.g., Gong et al., 2021; Holbrook et al., 2013; Sheen et al., 2009; Tang et al., 2020) but also the internal wave regime (e.g., Dickinson et al., 2017; Sheen et al., 2009; Xiao & Meng, 2022). In this paper, the spectral slope of turbulent regime is not obvious (Figure 4), so we used slope spectra of internal wave regime to estimate diapycnal diffusivity.

2.3.1. Tracking Seismic Reflectors

To estimate the turbulent dissipation rate from seismic data, the isopycnal displacement must be obtained first. A key assumption is that the seismic reflectors follow the isopycnals. Seismic reflectors are well correlated with isotherms (Ruddick et al., 2009; Sallares et al., 2009). Krahmann et al. (2009) analyzed seismic reflection data and Yoyo CTD data collected simultaneously around a Mediterranean eddy. They found that when the wavelength of the reflector was less than 800 – 2,800 m, it could be approximated as an isopycnal.

Before tracking the reflectors, we normalized the amplitude of the entire seismic transect. Then searched for all seismic peaks and troughs with amplitudes greater than 0.2. We discarded reflectors shorter than 800 m, because too-short reflectors cannot satisfy the wavenumber range. Taking line 04 as an example, the tracking results are shown in Figure 4a. Finally, we subtracted a linear trend from each reflector as the displacement of the isopycnal.

We did not use the method of tracking instantaneous phase contours of the seismic reflectors recommended by Holbrook et al. (2013), because the phase-based tracking method will pick reflectors in local weak amplitude areas. While *S*/*N* in weak amplitude areas is too low, the phase-based tracking method can cause large errors in the estimated results. The amplitude-based tracking method in this paper can avoid this problem.

2.3.2. Spectral Analysis

Using the Welch method, we performed a 128-point discrete Fourier transform (DFT) on the displacement of each isopycnal (Figure 4) tracked above with a half-overlapping Hanning window (Bai et al., 2015; Fer et al., 2010). Then we obtain the power spectrum, that is, the isopycnal displacement spectrum ϕ_ζ. Subsequently multiply ϕ_ζ by $(2\pi k_x)^2$, to obtain the slope spectrum $\phi_{\zeta x}$. To remove the influence of stratification, we use the reference buoyancy frequency $N_0 = 3$ cph to normalize the slope spectrum and obtain $(N/N_0)\phi_{\zeta x}$, where N is the buoyancy frequency at the average depth of each tracked reflector. We average all the slope spectra to obtain the average slope spectrum $\langle (N/N_0)\phi_{\zeta x} \rangle$ (Figure 4). In the low wavenumbers, the spectrum is consistent with the internal wave model of Garrett and Munk (1975). In the middle wavenumbers, the spectral slope of the turbulent regime is not obvious (Figure 4). In the high wavenumbers, the spectrum has a spectral slope of 2, which is caused by noise. The drop in spectral energy between the turbulent regime and the noise regime is the result of filtering and de-noising (e.g., Tang et al., 2020, 2021, 2022). The wavenumbers of the internal wave regime for 03BA, 04, and 07B transects are 0.0013–0.0049, 0.0013–0.0062, and 0.0013–0.0037 cpm, respectively. The equation

$$\varepsilon = 7 \times 10^{-10} \frac{N^2}{N_0^2} \left\langle \frac{\phi_{\zeta_x}^{\mathrm{IW}}}{\phi_{\zeta_x}^{\mathrm{GM}}} \right\rangle^2 \tag{2}$$

can be used to estimate turbulent dissipation rate attributable to internal wave breaking (Gregg, 1989; Sheen et al., 2009), where $N_0 = 3$ cph, $\phi_{\zeta_x}^{\mathrm{GM}}$ and $\phi_{\zeta_x}^{\mathrm{IW}}$ are the slope spectra of GM75 (Garrett & Munk, 1975) and internal wave regime, respectively. $\langle \cdot \rangle$ denotes the average calculated over the wavenumber bandwidth. This equation is accurate to within a factor of two (Gregg, 1989; Sheen et al., 2009). Following the method of Osborn (1980), we get the diapycnal diffusivity

$$K_\rho = \Gamma \varepsilon / N^2 \tag{3}$$

Here, we take the mixing efficiency Γ as an empirical constant of 0.2. To increase continuity, we interpolate and smooth the diffusivities (Figure 4e).

2.4. Estimating Diffusivity Using ADCP/CTD Data

To verify the accuracy of estimating the diffusivity using seismic data, a comparison was made from the diffusivity calculated using the ADCP-derived current velocity data and historical CTD data. The turbulent dissipation rate calculated using fine-scale parameterization (Gregg et al., 2003; Kunze et al., 2006) is

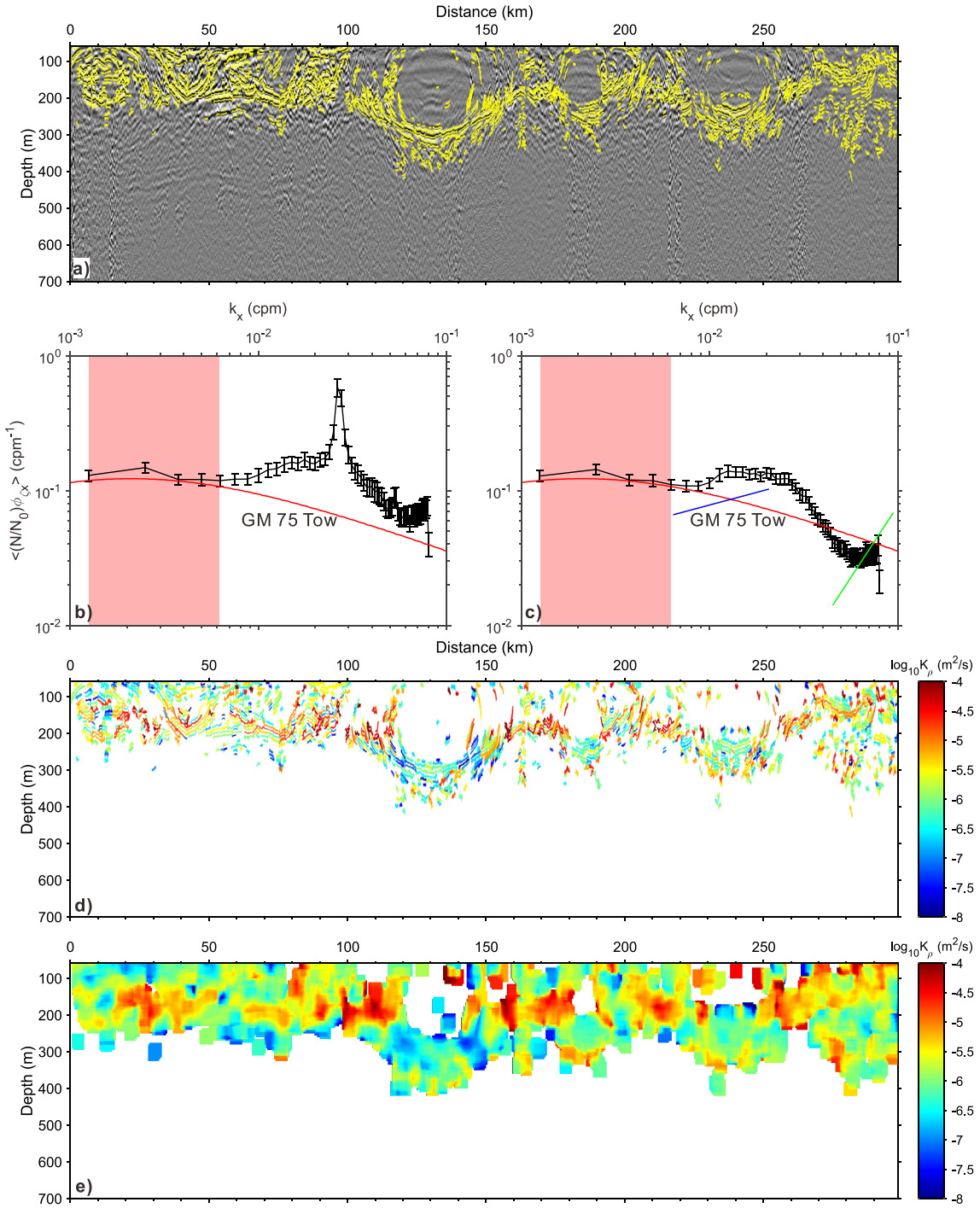

Figure 4. Spectral analysis, taking line 04 as an example. (a) Automatically tracked reflectors (yellow curves) overlaid on seismic images (gray). (b) and (c) are the average slope spectra with and without harmonic noise, respectively. The black vertical lines are the 95% confidence intervals. The red curves are GM75 spectra (Garret & Munk, 1975). The blue line and green line are the theoretical spectral slopes of turbulence (+1/3) and noise (+2), respectively. The red rectangle represents the fitting wavenumber range in the internal wave regime. (d) The estimated diapycnal diffusivity for each reflector. (e) The diapycnal diffusivities after interpolation and smoothing.

$$\varepsilon = \varepsilon_0(N, \phi_{\text{shear}}, \phi_{\text{strain}}) \times L(f, N) \tag{4}$$

where $\varepsilon_0(N,\phi_{\text{shear}},\phi_{\text{strain}})$ is the turbulent dissipation rate at the 30° GM model reference latitude, depends on stratification (N) and on internal wave characteristics (in terms of spectra of vertical shear, ϕ_{shear}, and of vertical strain,

21699291, 2023, 10, Downloaded from https://agupubs.onlinelibrary.wiley.com/doi/10.1029/2023JC019964 by Tongji University, Wiley Online Library on [05/09/2024]. See the Terms and Conditions (https://onlinelibrary.wiley.com/terms-and-conditions) on Wiley Online Library for rules of use; OA articles are governed by the applicable Creative Commons License

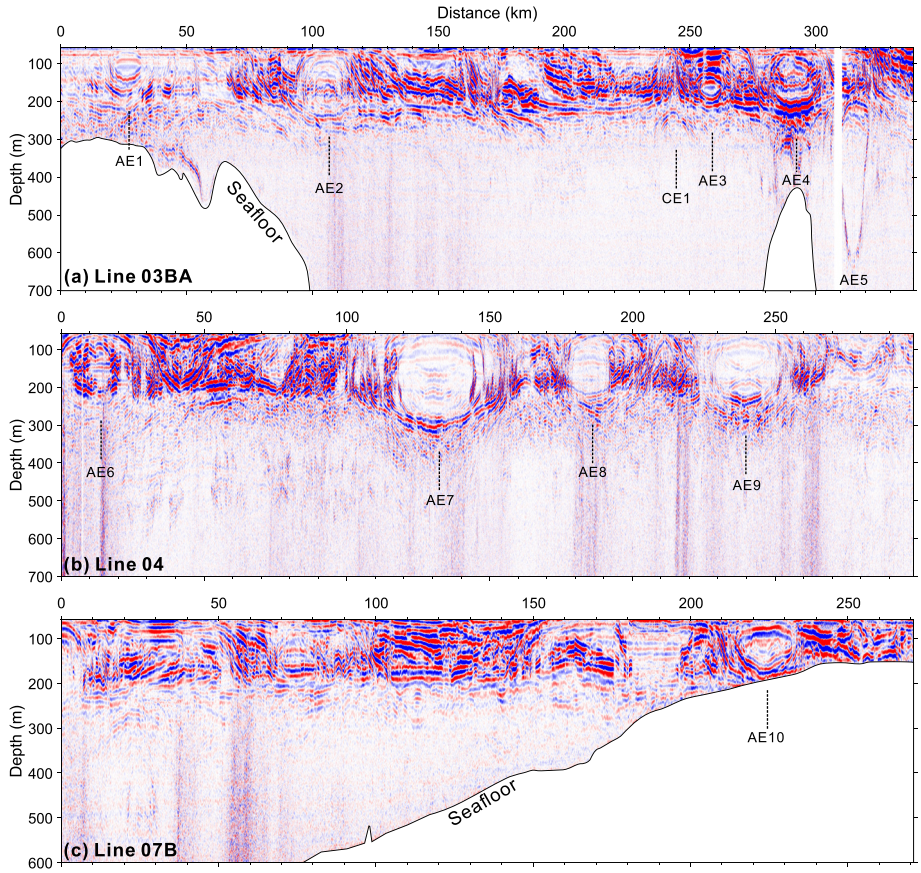

Figure 5. Seismic images of (a) lines 03BA, (b) 04, and (c) 07B. Eddy numbers are labeled.

ϕ_{strain}), $L(f,N)$ depends on the latitude (i.e., Coriolis frequency, f) and stratification. The vertical shear spectrum and strain spectrum are calculated from ADCP-derived current velocity and CTD-derived buoyancy frequency, respectively. Shear and strain profiles are both divided into depth windows of 200 m with a step of 50 m. The shear and strain spectra are integrated in wavenumber ranges corresponding to wavelengths 50–200 m and 20–200 m, respectively. The turbulent dissipation rate here is calculated using *mixsea* python toolbox (Voet et al., 2022). Finally, we can get the diffusivity K_ρ using Equation 3. Note that the vertical strain was calculated using temperature and salinity derived from CTD No.10 (Figures 1b and 3).

3. Results

3.1. Eddies Identified From Seismic Images and Current Velocity Data

Seismic images of seawater columns represent the vertical gradient of physical parameters such as temperature and salinity in the ocean interior and can be simply regarded as the smoothed vertical temperature gradient (Ruddick et al., 2009). As shown in Figure 5, eddies on seismic images appear as lens-shaped, bowl-shaped, or elliptical (e.g., Biescas et al., 2008; Gula et al., 2019; Song et al., 2011). To identify eddies more accurately in seismic images, current velocity data are combined. Figure 6 shows the velocity component U_n, which is perpendicular to transects. On the U_n images, a pair of adjacent "negative left and positive right" velocity areas represent an anticyclonic eddy (AE); on the contrary, a pair of adjacent "positive left and negative right" velocity areas represent a cyclonic eddy (CE).

Line 03BA was acquired from northwest to southeast, crossing the Chukchi Plateau, Northwind Basin, and Northwind Ridge, and finally reaching the Canada Basin. As shown in Figure 5a, the reflections can be divided into two zones vertically: Above about 250 m is a strong reflection zone, and below is a weak reflection zone. The strong reflection zone in the upper roughly corresponds to the halocline, which is related to the cold winter water (WW) and residual winter water (RWW); the weak reflection in the lower mainly corresponds to the warm Atlantic water (AW). The details of these water masses are showed in Section 2 of S. Yang et al. (2022).

21699291, 2023, 10, Downloaded from https://agupubs.onlinelibrary.wiley.com/doi/10.1029/2023JC019964 by Tongji University, Wiley Online Library on [05/09/2024]. See the Terms and Conditions (https://onlinelibrary.wiley.com/terms-and-conditions) on Wiley Online Library for rules of use; OA articles are governed by the applicable Creative Commons License

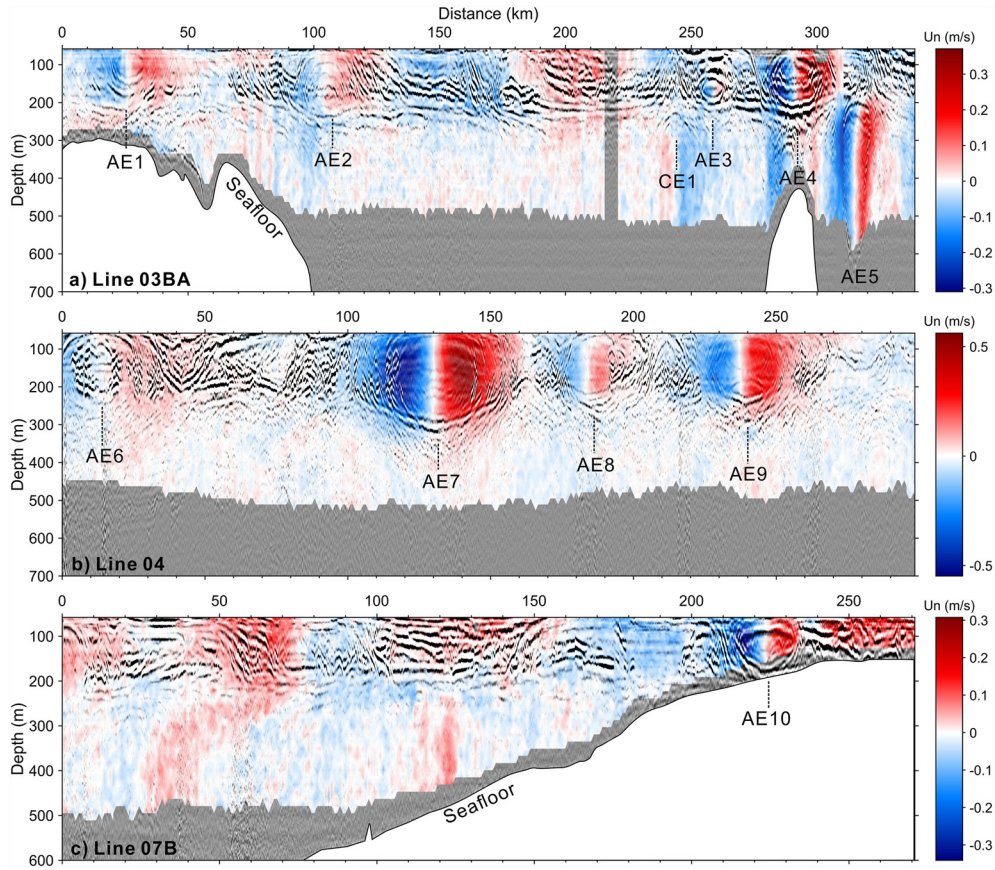

Figure 6. The normal velocity U_n sections (in color) are overlaid on the seismic images (gray) of (a) lines 03BA, (b) 04, and (c) 07B. Red and blue indicate outward and inward respectively. Eddy numbers are labeled.

Combining concurrent seismic images and current velocity images (Figures 5a, 6a, and 7), four anticyclonic eddies were identified in the shallow strong reflection zone of the 03BA transect, as intra-halocline eddies; a cyclonic eddy and an anticyclonic eddy were identified in the deep weak reflection zone, as Atlantic water eddies. The information on these eddies is shown in Table 2. As shown in Figure 7a, line 03BA did not pass through the centers of anticyclones AE1 and AE2. The eddy AE1 has a thick bottom edge, while the top edge is not obvious. The eddy AE2 has multi-layer concentric edges, similar to a Mediterranean eddy found by Biescas et al. (2008). The eddy AE3 has a small transparent core and thick edges, indicating that its core water has been mixed sufficiently with the background water. AE4 was located right above the Northwind Ridge and seemed to have a vertical double-core structure. Cyclone CE1 and anticyclone AE5 are located in Atlantic water. CE1 only appears as an upward convex reflection on its top edge in the seismic image. AE5 appears as bowl-like and has very thin lateral edges, and the reflection of the eddy core is very weak, indicating a quite homogeneous core water mass.

Line 04 is roughly parallel to line 03BA, but with the opposite acquisition direction, starting from the Canada Basin, crossing the Northwind Ridge and Northwind Basin, and ending at the Chukchi Plateau. As shown in Figures 5b, 6b, and 7, four eddies were captured by line 04, all of which were anticyclonic (Table 2). The center of AE6 was not crossed by the seismic line (Figure 7). The eddy AE6 showed multi-layer reflections, but with nearly horizontal reflections within each layer. The eddy AE7 was a large anticyclonic eddy with a maximum velocity of 0.6 m s^{-1} and had large-slope tilted reflectors on both sides of its core. S. Yang et al. (2022) studied eddy AE7 in detail and found that the eddy core was very uniform and rigidly rotating and that the reflections on both sides of the core were similar to the spiral rainbands of tropical cyclones, which was a kind of submesoscale structure. The eddy AE8 was close to AE7, but its center was not crossed by the seismic line either, so its velocity value was small and its core water was relatively uniform. The eddy AE9 has a double-core structure vertically. The double-core eddy has been reported by Zhao and Timmermans (2015), Biescas et al. (2008), and S. Yang et al. (2021). Unlike eddy 04-AE4, Zhao and Timmermans (2015) found that the double-core eddy, with two cores at depths

21699291, 2023, 10, Downloaded from https://agupubs.onlinelibrary.wiley.com/doi/10.1029/2023JC019964 by Tongji University, Wiley Online Library on [05/09/2024]. See the Terms and Conditions (https://onlinelibrary.wiley.com/terms-and-conditions) on Wiley Online Library for rules of use; OA articles are governed by the applicable Creative Commons License

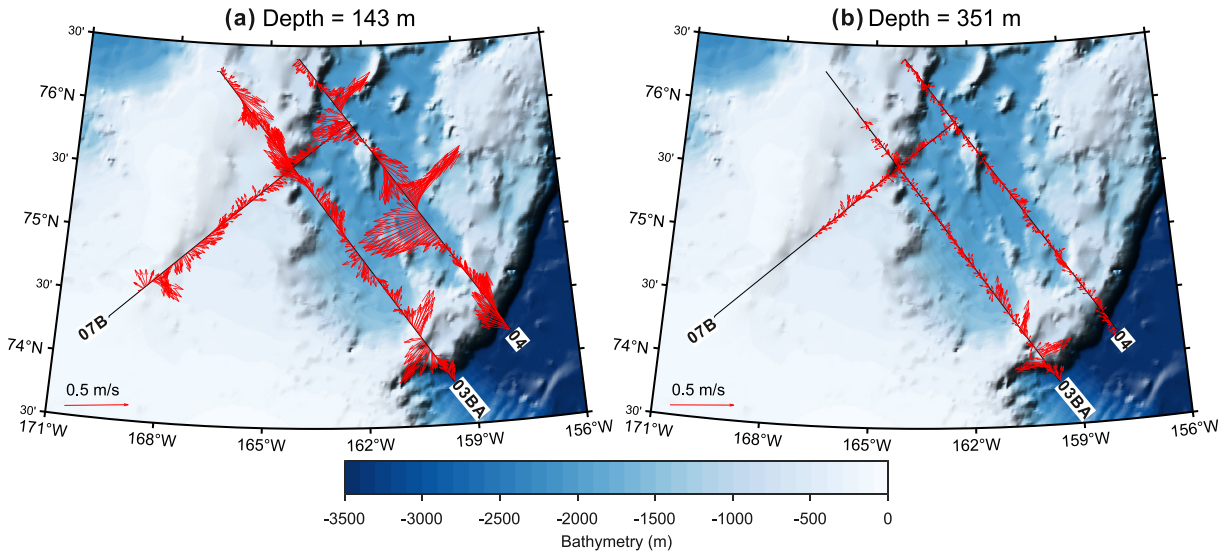

Figure 7. The horizontal current velocity (red arrows) was measured by ADCP simultaneously with seismic lines at depths of (a) 143 m and (b) 351 m. The black lines are ship tracks. Seismic line numbers are labeled.

of 300 and 500 m respectively, was located in deeper Atlantic water. Zhao and Timmermans (2015) suggested that the double-core eddy might be formed by frontal instability. Biescas et al. (2008) and S. Yang et al. (2021) suggested that the double-core structure might be due to the fact that the seismic line did not cross the eddy core or that the eddy existed for too long so that its core was intruded by external water masses. The core of 04-AE4 was crossed by the seismic line (Figure 7), so we can rule out the first possibility.

Line 07B starts from the Northwind Basin and ends at the Chukchi Shelf. Compared with lines 03BA and 04, the seismic image of line 07B is simpler, with only one eddy reflection AE10 (Figure 5c). The left half of the transect reveals the chaotic current directions (Figure 6c). The eddy AE10 is overall bowl-shaped and very close to the shelf. Possibly due to the interaction with the seafloor, the seaward edge of AE10 is thicker, while the shoreward edge is narrower (Figure 5c). The bottom of AE10 is asymmetric, which may also be caused by the interaction with the seafloor.

3.2. Distribution of Diffusivity Estimated From Seismic Images

Due to the lack of reflectors below the halocline, it is difficult to obtain the diffusivities of eddies CE1 and AE5 in the Atlantic water. The diffusivities, estimated from seismic images, of the remaining 9 eddies are shown in

Table 2
Information on Eddies Recognized From Seismic and Current Velocity Data

Eddy	Rotation	Center location (km)	Center depth (m)	Horizontal scale (km)	Description
AE1	AE	25	104	30	Thick bottom edge
AE2	AE	105	157	40	Concentric reflection
AE3	AE	257	169	20	The transparent core is very small; edges are very thick
AE4	AE	290	134	35	Double-core reflection; above the ridge
CE1	CE	242	353	20	Only top edge reflection
AE5	AE	313	380	25	Perfect bowl shape; very thin edges; transparent core
AE6	AE	13	127	30	Multi-layer edges; reflection at the edges near horizontal
AE7	AE	132	157	60	The edges have multiple reflection zones with large slopes; transparent core
AE8	AE	184	170	30	Transparent core
AE9	AE	240	159	40	Double-core structure
AE10	AE	224	114	30	Above the shelf; asymmetric

21699291, 2023, 10, Downloaded from https://agupubs.onlinelibrary.wiley.com/doi/10.1029/2023JC019964 by Tongji University, Wiley Online Library on [05/09/2024]. See the Terms and Conditions (https://onlinelibrary.wiley.com/terms-and-conditions) on Wiley Online Library for rules of use; OA articles are governed by the applicable Creative Commons License

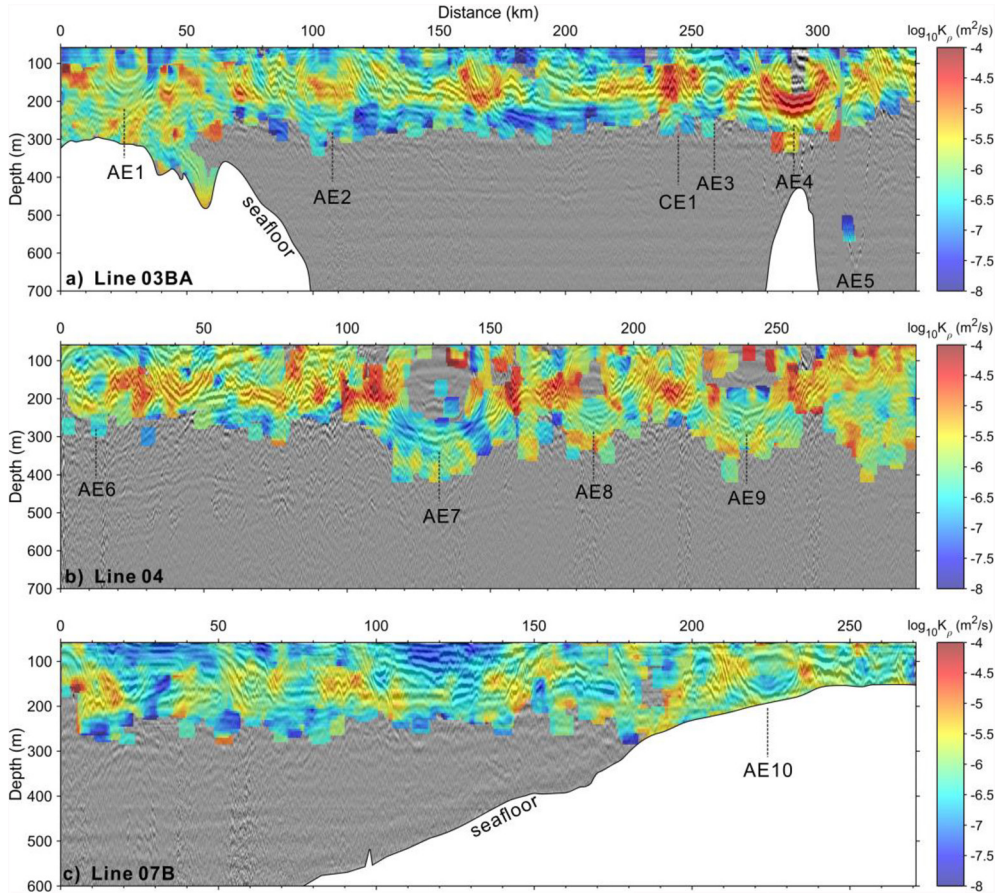

Figure 8. The diapycnal diffusivities in logarithm $\log_{10} K_\rho$ (in color), estimated using seismic data of lines (a) 03BA, (b) 04 and (c) 07B, are overlaid on seismic images (gray). Eddy numbers are labeled.

Figure 8. The diffusivities at the edges of these eddies were generally high, compared with background water. The diffusivities at the edges of eddies AE3 (left edge), AE4 (left, right, and bottom edges), and AE7 (left, right, and top edges) can be up to 10^{-4} m^2 s^{-1}; the diffusivities at the edges of eddies AE1 (left and right edges), AE6 (right edge), AE8 (left and right edges), and AE9 (left, right, and top edges) can exceed 10^{-5} m^2 s^{-1}; the diffusivities at the edges of eddies AE2 and AE10 were around $10^{-5.5}$ m^2 s^{-1}.

Except for at the edges of these eddies, the diffusivities at the strong currents (see Figure 6 for current velocities) were also high, such as at ~70 km, and 160–170 km in line 03BA, and around 10, 60, and 90 km in line 07B (Figures 8a and 8c). These high diffusivities may be due to strong current shear, and the latter can cause the tilting of isopycnals (i.e., seismic reflectors).

Moreover, the diffusivities above the Chukchi Plateau (the left part of line 03BA, Figure 8a) were also high, around $10^{-5.5}$ m^2 s^{-1}, which were greater than those at the rest of the area apart from areas in the presence of eddies and strong currents. This result is consistent with Shaw and Stanton (2014), who observed enhanced turbulent diffusivities, also around $10^{-5.5}$ m^2 s^{-1}, over the Chukchi Borderlands bathymetry.

3.3. Distribution of Diffusivity Estimated From ADCP/CTD Data

To validate the diffusivity estimated from seismic data, here shows the diffusivities (Figure 9) calculated from ADCP-derived current velocity and historical CTD-derived temperature and salinity data, using fine-scale parameterization.

As can be seen in Figure 9, the diffusivities at the edges of most of these eddies can be up to 10^{-5}–10^{-4} m^2 s^{-1}, especially at the bottom edges. These high diffusivities estimated from ADCP/CTD data were consistent with those estimated from seismic data (Figure 8). Though the diffusivities (~$10^{-5.5}$ m^2 s^{-1}) of the eddy AE10 were

21699291, 2023, 10, Downloaded from https://agupubs.onlinelibrary.wiley.com/doi/10.1029/2023JC019964 by Tongji University, Wiley Online Library on [05/09/2024]. See the Terms and Conditions (https://onlinelibrary.wiley.com/terms-and-conditions) on Wiley Online Library for rules of use; OA articles are governed by the applicable Creative Commons License

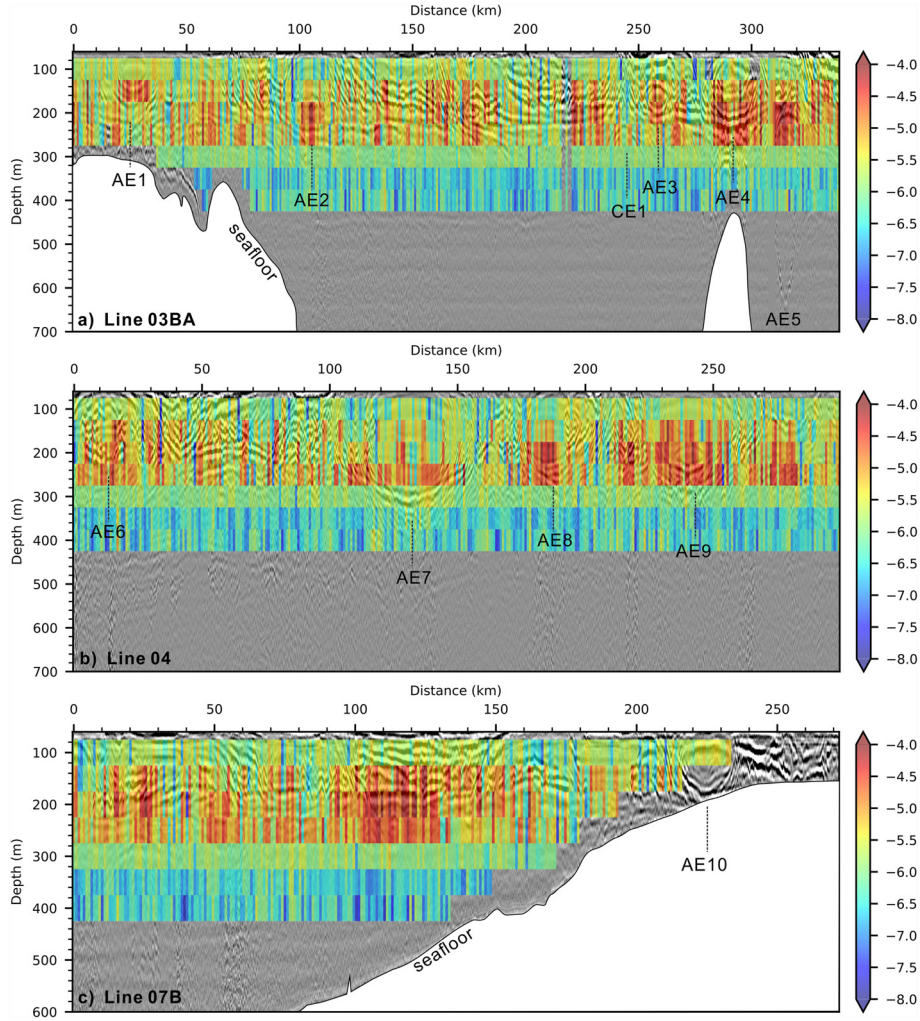

Figure 9. The diapycnal diffusivities (unit: $m^2\ s^{-1}$) in logarithm $\log_{10} K_\rho$ (in color), estimated using ADCP/CTD data, of lines (a) 03BA, (b) 04, and (c) 07B are overlaid on seismic images (gray). Eddy numbers are labeled.

incomplete, they were also broadly consistent with the results estimated from seismic data (Figure 8c). However, even though the results estimated by these two methods are broadly consistent, there are some differences in diffusivities estimated between seismic and velocity data. For example, diffusivities at the left part of line 07B estimated from ADCP/CTD data were greater than the results estimated from seismic data. Given that these two results come from two different data sources, we believe that this difference is reasonable.

Moreover, the probability density functions (PDFs) of diffusivities in logarithm $\log_{10} K_\rho$ of these three sections (Figure 10), show that the mean values of $\log_{10} K_\rho$ are all about $-6\ m^2\ s^{-1}$. The results estimated from ADCP/CTD data are slightly greater than those estimated from seismic data, which is acceptable (Figure 10). The consistency of estimated diffusivities, between seismic data and ADCP/CTD data, indicates that seismic-estimated diffusivities are appropriate and reliable.

4. Discussion

4.1. Mesoscale Eddies in the Western Arctic Ocean

Zhao et al. (2014, 2016) conducted a systematic study on eddies in and around the Canada Basin. Zhao et al. (2014) observed the Arctic halocline eddies using the 10-years Ice-Tethered Profilers (ITPs) and found 127 mesoscale eddies, 95% of which were anticyclonic eddies, and most of which were cold eddies. Zhao et al. (2016) used ITPs observations from 2005 to 2015 to detect 243 eddies in and around the Canada Basin, 98% of them were

21699291, 2023, 10, Downloaded from https://agupubs.onlinelibrary.wiley.com/doi/10.1029/2023JC019964 by Tongji University, Wiley Online Library on [05/09/2024]. See the Terms and Conditions (https://onlinelibrary.wiley.com/terms-and-conditions) on Wiley Online Library for rules of use; OA articles are governed by the applicable Creative Commons License

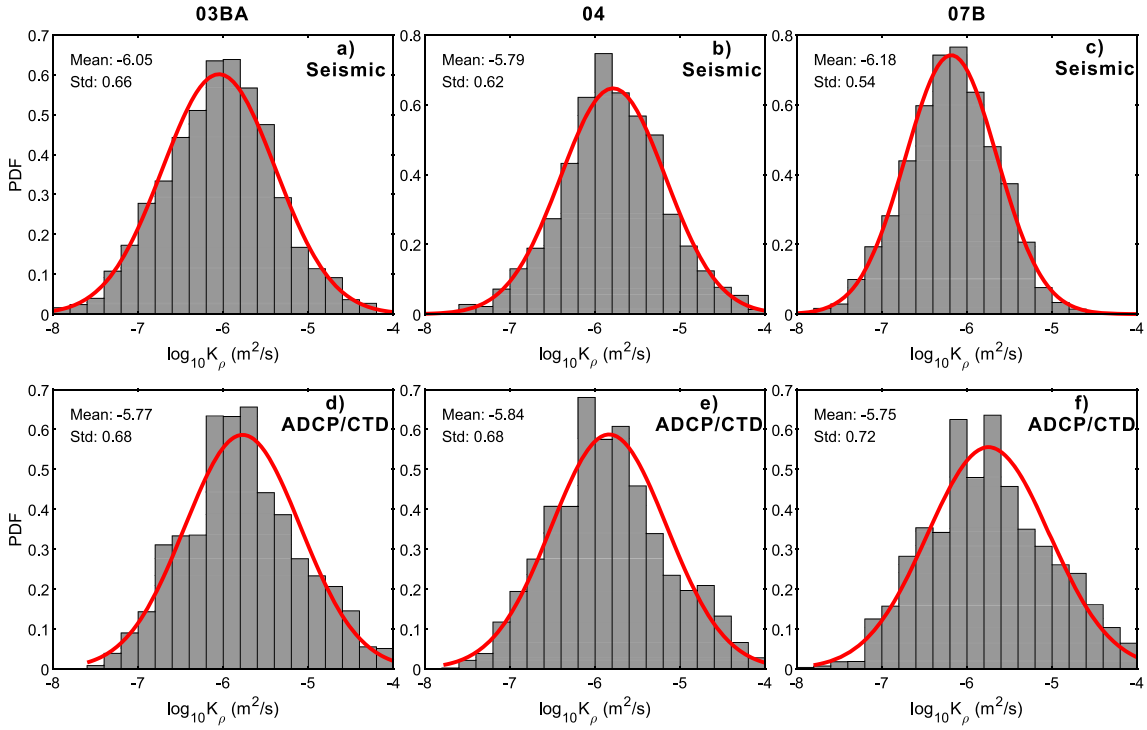

Figure 10. The probability density functions (PDFs) of diffusivities in logarithm estimated from (a–c) seismic data and (d–f) ADCP/CTD data of lines 03BA, 04, and 07B, respectively. The red curves are the Gaussian fitting of these PDFs. The values at the top left corner of each panel denote their mean values and standard deviations.

anticyclones and 70% were cold eddies. The spatial density of these eddies was the highest in the western and southern edges of the basin, which was close to the boundaries of the topography and the Beaufort Gyre.

In our work, 11 eddies were identified on the three seismic reflection sections combined with the concurrent current velocity data. Among these eddies, 10 eddies (91%) were anticyclonic and one eddy was cyclonic; 9 eddies (82%) had their core depths in the shallow halocline (i.e., intra-halocline eddies), and the remaining 2 were in the deep Atlantic water (i.e., Atlantic water eddies). These results are consistent with previous studies (e.g., Zhao et al., 2014, 2016), that is, the halocline eddies are mainly anticyclonic. These eddies mostly have horizontal scales of 20–40 km (Figure 11), greater than the local Rossby deformation radius (~10–15 km, Nurser & Bacon, 2014) around the Northwind Basin, hence belonging to mesoscale eddies. Note that the horizontal scales here, including the core and edges, are determined by the influence range of the eddy current velocity, rather than the core diameter determined by the maximum azimuthal velocity of eddies (e.g., Timmermans et al., 2008; Zhao et al., 2014). Therefore, the horizontal scales here are larger than the diameters of eddies previously studied (e.g., Timmermans et al., 2008; Zhao et al., 2014). While the eddy AE7 has the maximum horizontal scale (~60 km) of these eddies, which is consistent with a baroclinic eddy above the Chukchi slope observed by Kawaguchi et al. (2012).

The total length of horizontal scales of these 11 eddies is ~360 km, which occupies ~40% of the total length of three seismic lines (Table 2). Especially, the total length of horizontal scales of eddies in the first two seismic lines occupies ~52% of the lengths of the two seismic lines. This indicates that eddies at the Chukchi Borderlands were widespread. This result is comparable to Manley and Hunkins (1985), who estimated that mesoscale eddies occupy at least 25% of the sea surface area (i.e., 50% of the horizontal length) of the Beaufort Sea.

4.2. Formation Mechanisms of These Eddies

Numerous studies have analyzed the formation mechanism and source of eddies in the western Arctic Ocean. The formation mechanism of shallow halocline eddies includes the local increase of water density caused by the icing of polynyas (e.g., Muench et al., 2000), the instability of front regions (e.g., Timmermans et al., 2008; X. Zhang et al., 2019), the instability of boundary currents (e.g., Spall et al., 2008), and the interaction between currents and topography (e.g., D'Asaro, 1988).

21699291, 2023, 10, Downloaded from https://agupubs.onlinelibrary.wiley.com/doi/10.1029/2023JC019964 by Tongji University, Wiley Online Library on [05/09/2024]. See the Terms and Conditions (https://onlinelibrary.wiley.com/terms-and-conditions) on Wiley Online Library for rules of use; OA articles are governed by the applicable Creative Commons License

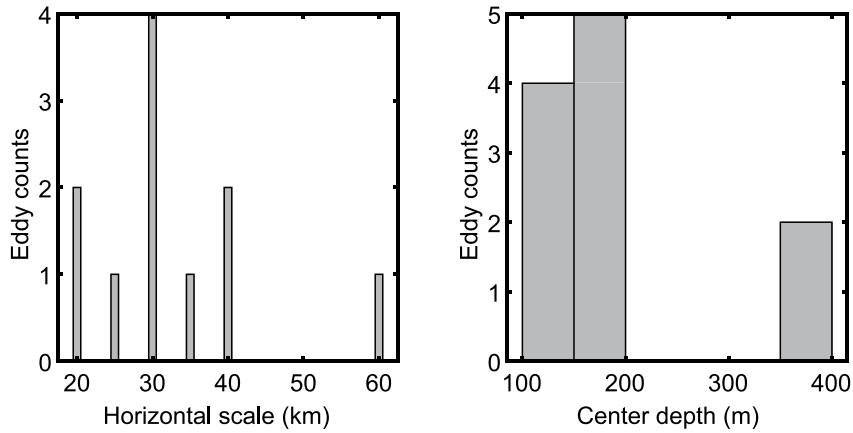

Figure 11. Statistics of (left panel) horizontal scales and (right panel) center depths of 11 mesoscale eddies. See Table 2 for more details.

Different from the eddies in the Canada Basin center mainly studied by previous researchers, the eddies in this paper are mainly concentrated around the Northwind Basin (including the Chukchi Plateau, the Chukchi Shelf, and the Northwind Ridge), that is, located at the boundary of the Canada Basin. The topography and currents here are both complex (Figure 1), with a westward Chukchi slope current and Beaufort Gyre, as well as an eastward Chukchi shelf jet, resulting in strong baroclinic instability (e.g., Spall et al., 2008) and a high incidence of eddies (e.g., Zhao et al., 2016). Therefore, these intra-halocline eddies may be mainly caused by the baroclinic instability of boundary currents. Due to the lack of in situ temperature and salinity observations in the center of these eddies, we cannot determine whether they are generated locally or generated from the distance and carried here by background currents.

Furthermore, it is difficult for us to track the trajectories of these subsurface eddies by satellite observations. Different observation methods are biased toward particular aspects of the complex eddy field (Kubryakov et al., 2021): ITPs and seismic data reveal the interior eddy field (e.g., S. Yang et al., 2022; Zhao et al., 2016), while satellite altimetry only detects large-scale eddies (Kubryakov et al., 2021). These subsurface eddies with relatively smaller scales are hard to detect by satellites. Fortunately, S. Yang et al. (2022) observed twice the eddy AE7 7 days apart. Their results showed that during the observation, this eddy moved westward at a speed of $\sim$1 cm s^{-1}. This indicates eddies here may move with boundary currents.

4.3. Enhanced Mixing at the Edges of These Eddies

In this study, the estimated turbulent diffusivities at the edges of intra-halocline eddies in the western Arctic Ocean can be up to 10^{-4} m^2 s^{-1} (Figure 8), which is not only higher than the statistical average of 10^{-5} m^2 s^{-1} in the global open ocean (e.g., Munk & Wunsch, 1998) but also far exceeds the background values of 10^{-6}–10^{-5} m^2 s^{-1} in the Arctic Ocean halocline (e.g., Fer, 2009; Shaw & Stanton, 2014).

Compared with the results of previous works in the Arctic (e.g., Fer, 2009; Schulz et al., 2023), the enhanced diffusivities at the edges of these eddies seem too large. But it is worth noting that their observation sites (e.g., Fer, 2009; Schulz et al., 2023) were very close to the North Pole, located at the center of the Arctic basin, where the ice is thick and the currents are weak. Shaw and Stanton (2014) found that vertical diffusion in the western Arctic Ocean halocline proceeds at molecular rates in the deep basins and away from topographic features. While our observation site is located at the ice-free Chukchi Borderlands (at the edge of the Canada Basin; see Figure 1) in September, where the topography is shallow and rough, currents are strong and complex, and with frequent eddies. Besides, Shaw and Stanton (2014) thought the Chukchi Borderlands is a hot spot for vertical heat transport, where the turbulent diffusivities can be greater than 10^{-5} m^2 s^{-1}. Zhong et al. (2018) and Lin et al. (2022) also achieved similar results to Shaw and Stanton (2014). The average diffusivities derived from three seismic sections are all $\sim 10^{-6}$ m^2 s^{-1} (Figure 10), which is consistent with the average diffusivities at the Chukchi Borderlands observed by Shaw and Stanton (2014). Apart from that, our results are roughly consistent with those estimated from ADCP/CTD data using fine-scale parameterization (Figures 9 and 10). Therefore,

21699291, 2023, 10, Downloaded from https://agupubs.onlinelibrary.wiley.com/doi/10.1029/2023JC019964 by Tongji University, Wiley Online Library on [05/09/2024]. See the Terms and Conditions (https://onlinelibrary.wiley.com/terms-and-conditions) on Wiley Online Library for rules of use; OA articles are governed by the applicable Creative Commons License

21699291, 2023, 10, Downloaded from https://agupubs.onlinelibrary.wiley.com/doi/10.1029/2023JC019964 by Tongji University, Wiley Online Library on [05/09/2024]. See the Terms and Conditions (https://onlinelibrary.wiley.com/terms-and-conditions) on Wiley Online Library for rules of use; OA articles are governed by the applicable Creative Commons License

taking into account the above, we believe that the enhanced diffusivities (can be up to 10^{-4} m^2 s^{-1}) at the edges of these intra-halocline eddies are reliable. The reasons of these enhanced diffusivities will be analyzed later.

As a weakly mixing region, the Arctic halocline with strong stratification is essential in isolating the sea surface and the sea ice from the underlying warm Atlantic Water (e.g., Carmack et al., 2015; Fer, 2009). The enhanced diapycnal mixing at the edges of intra-halocline eddies can effectively increase the upward heat flux, thus transferring the heat of the warm Atlantic water below to the surface, which may further promote the melting of surface sea ice. Similar to Fine and Cole (2022), we speculate that this forms a feedback cycle: (a) The decline in sea ice cover makes the Arctic Ocean more energetic, generating more eddies; (b) more eddies enhance the vertical diffusivities, thus increasing the upward heat flux from warm Atlantic water; (c) the enhanced upward heat flux further promotes the melting of sea surface ice.

4.4. Mixing Mechanisms of the Enhanced Diffusivities

4.4.1. Shear Instabilities

Shear instabilities occur when the shear in a flow is relatively high compared to the local stratification (N), leading to overturning and turbulent mixing (Thorpe, 2007). The relative strength of shear to stratification can be characterized by the Richardson number, $Ri = N^2/S^2$, where $S^2 = U_z^2 = (\partial u/\partial z)^2 + (\partial v/\partial z)^2$ is the vertical shear of horizontal current velocity. For stable, inviscid, non-diffusive, two-dimensional horizontal fluids, shear instability can only occur when Ri is less than 1/4 (Thorpe, 2007). However, actual seawater motion is complex, making it difficult to define a critical Ri. Due to the rotation of eddies, the shear above and below their cores can be enhanced (e.g., Fine et al., 2018). Figure 12 shows the vertical shear derived from ADCP, that is, U_z^2. It is obvious that strong shear exists at the top and bottom edges of almost all eddies. The distribution of Ri is not provided here because using only the background N of the ambient water can lead to significant errors. The enhanced mixing at the top or/and bottom edges of eddies (e.g., AE4, AE7, AE9, and AE10), may be due to these strong shears. However, there are no obviously enhanced diffusivities at the top and bottom edges of some eddies with strong shears at the top and bottom edges. We speculate that this is because the buoyancy frequency used in the estimation is the background values, obtained from historical CTDs, rather than the in situ values. Another possibility is, although the shear is large, the actual Ri is not small due to the large N (e.g., Hua et al., 2013; Zhao et al., 2014) at the bottom and top edges of these eddies.

4.4.2. Submesoscale Motions

In our work, the enhanced diffusivities are more common at the left or/and right edges of these eddies (e.g., AE1, AE3, AE4, AE6, AE7, AE8, and AE9; Figure 8). This may be attributed to submesoscale motions at the lateral edges of these eddies (e.g., Qi et al., 2020; Wang et al., 2022; Q. Yang et al., 2017). Submesoscale motions surrounding mesoscale eddies can cause strong vertical velocities, thus elevating diapycnal mixing (e.g., Wang et al., 2022). Q. Yang et al. (2017) observed enhanced mixing around three mesoscale eddies in the South China Sea by direct microstructure measurements, and they thought this is due to the strong submesoscale motions in the periphery of these eddies. We can see many submesoscale features at the lateral edges of these eddies (e.g., AE3, AE4, AE7, and AE9), which present as narrow reflectors with widths of about a few kilometers (Figure 5). Of them, there are the most obvious submesoscale features around AE7, which was analyzed by S. Yang et al. (2022). They called this kind of submesoscale features spiral bands or spiral arms (see Figures 6 and 12 of S. Yang et al., 2022). Similar submesoscale phenomena also were analyzed in detail by Ménesguen et al. (2012) and Z. Zhang and Qiu (2020).

5. Summary

Using concurrently collected seismic reflection data and ADCP-derived current velocity, this study identified 11 mesoscale eddies in the ice-free Chukchi Borderlands of the western Arctic Ocean. Of them, 10 eddies were anticyclonic and one eddy was cyclonic; 9 were intra-halocline eddies and 2 were Atlantic water eddies. This means most of them are anticyclonic eddies in the halocline, which is consistent with previous studies (Zhao et al., 2014, 2016). The total length of horizontal scales of these 11 eddies is ~40% of the total length of three seismic lines, which indicates that eddies were widespread at the Chukchi Borderlands. These eddies may be caused by the baroclinic instability of boundary currents.

Diapycnal diffusivities estimated from seismic data were enhanced and can be up to 10^{-4} m^2 s^{-1} at the edges of these eddies, compared with the average values (~10^{-6} m^2 s^{-1}) at the Chukchi Borderlands. Seismic-estimated

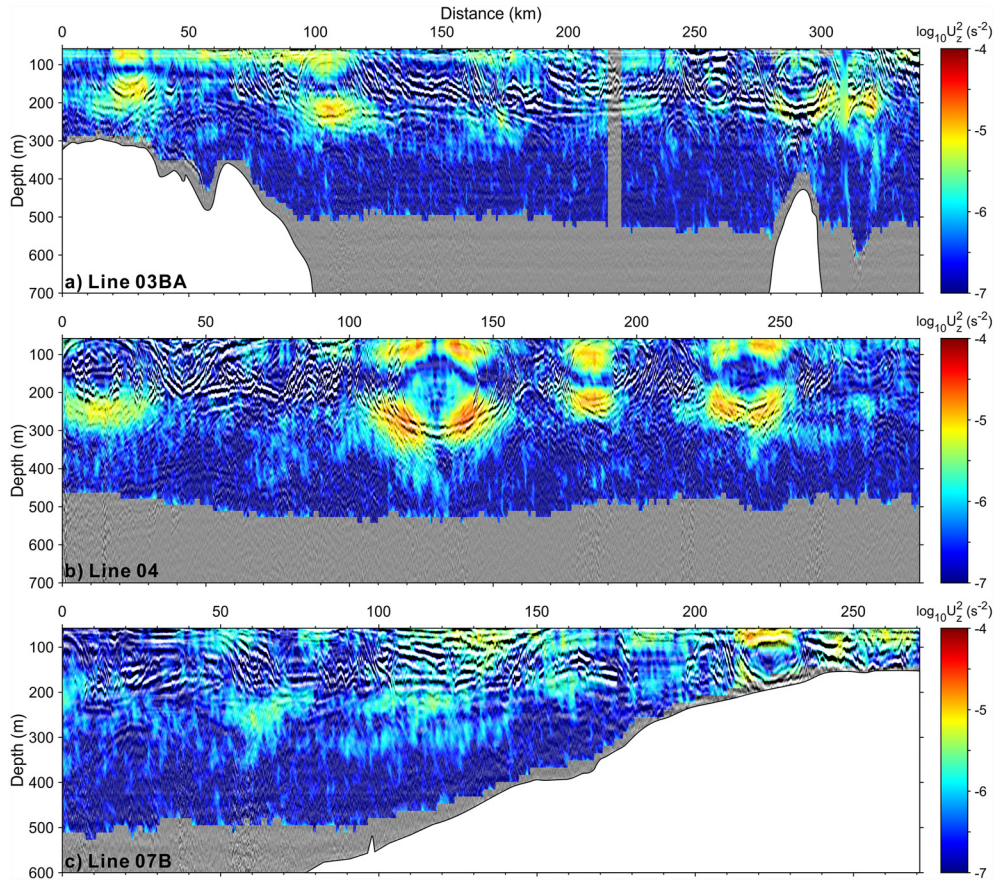

Figure 12. The vertical shears (in color) of horizontal current velocity derived from ADCP are overlaid on seismic sections (a) 03BA, (b) 04, and (c) 07B. The vertical shears are displayed on a logarithmic scale.

diffusivities were validated by fine-scale parameterization using ADCP-derived velocity data, and temperature and salinity from historical CTDs. The results of these two methods are roughly consistent. Enhanced diapycnal diffusivities at the edges of eddies may be attributed to shear instabilities at the top and bottom edges and to submesoscale motions at the lateral edges of these eddies. Finally, we highlight the enhanced vertical mixing at the edges of eddies in the halocline can increase the upward heat flux, thus transferring the heat of the warm Atlantic water below to the surface, which may further promote the melting of surface sea ice.

Data Availability Statement

The raw multi-channel seismic data are provided by MGDS (the Marine Geoscience Data System), are available from Coakley (2014). The preprocessed ADCP data are available from S. Yang et al. (2023). The historical CTD data are from World Ocean Database (Boyer et al., 2018). The diffusivities are calculated by using ADCP/CTD data with *mixsea* python toolbox (Voet et al., 2022).

Acknowledgments
The ADCP-derived velocity data were preprocessed by Andrew Frambach and Jules Hummon from University of Hawaii. We thank them for their assistance in processing the ADCP data. We are very grateful to all scientists and crew members of cruise MGL1112 for their contributions to the acquisition of multichannel seismic and ADCP data. The seismic and ADCP data acquisition was funded by the US National Science Foundation (Grant ARC09-09568), and this work was funded by the National Natural Science Foundation of China (Grants 42176061, 41976048).

References

Bai, Y., Song, H., Dong, C., Liu, B., Chen, J., & Geng, M. (2015). Extraction of mixing parameters by seismic oceanography and applications: Case study of the internal waves in South China Sea and Mediterranean eddy. *Chinese Journal of Geophysics-Chinese Edition*, *58*(7), 2473–2485.

Biescas, B., Sallares, V., Pelegri, J. L., Machin, F., Carbonell, R., Buffett, G., et al. (2008). Imaging meddy finestructure using multichannel seismic reflection data. *Geophysical Research Letters*, *35*(11), L11609. https://doi.org/10.1029/2008GL033971

Boyer, T. P., Baranova, O. K., Coleman, C., Garcia, H. E., Grodsky, A., Locarnini, R. A., et al. (2018). World ocean database 2018 [Dataset]. https://www.ncei.noaa.gov/access/world-ocean-database-select/dbsearch.html

Carmack, E., Polyakov, I., Padman, L., Fer, I., Hunke, E., Hutchings, J., et al. (2015). Toward quantifying the increasing role of oceanic heat in sea ice loss in the New Arctic. *Bulletin of the American Meteorological Society*, *96*(12), 2079–2105. https://doi.org/10.1175/BAMS-D-13-00177.1

21699291, 2023, 10, Downloaded from https://agupubs.onlinelibrary.wiley.com/doi/10.1029/2023JC019964 by Tongji University, Wiley Online Library on [05/09/2024]. See the Terms and Conditions (https://onlinelibrary.wiley.com/terms-and-conditions) on Wiley Online Library for rules of use; OA articles are governed by the applicable Creative Commons License

Carpenter, J. R., & Timmermans, M. L. (2012). Deep mesoscale eddies in the Canada Basin, Arctic Ocean. *Geophysical Research Letters*, *39*(20), L20602. https://doi.org/10.1029/2012GL053025

Coakley, B. (2014). Multi-channel seismic shot data from the Chukchi Sea, Arctic Ocean, acquired during the R/V Marcus G. Langseth expedition MGL1112 (2011) [Dataset]. Interdisciplinary Earth Data Alliance (IEDA). https://www.marine-geo.org/tools/search/Files.php?data_set_uid=18256

D'Asaro, E. A. (1988). Generation of submesoscale vortices: A new mechanism. *Journal of Geophysical Research*, *93*(C6), 6685–6693. https://doi.org/10.1029/JC093iC06p06685

Dickinson, A., White, N. J., & Caulfield, C. P. (2017). Spatial variation of diapycnal diffusivity estimated from seismic imaging of internal wave field, Gulf of Mexico. *Journal of Geophysical Research: Oceans*, *122*(12), 9827–9854. https://doi.org/10.1002/2017JC013352

Falder, M., White, N. J., & Caulfield, C. P. (2016). Seismic imaging of rapid onset of stratified turbulence in the South Atlantic Ocean. *Journal of Physical Oceanography*, *46*(4), 1023–1044. https://doi.org/10.1175/jpo-d-15-0140.1

Fer, I. (2009). Weak vertical diffusion allows maintenance of cold halocline in the Central Arctic. *Atmospheric and Oceanic Science Letters*, *2*(3), 148–152. https://doi.org/10.1080/16742834.2009.11446789

Fer, I., Nandi, P., Holbrook, W. S., Schmitt, R. W., & Paramo, P. (2010). Seismic imaging of a thermohaline staircase in the western tropical North Atlantic. *Ocean Science*, *6*(3), 621–631. https://doi.org/10.5194/os-6-621-2010

Fine, E. C., & Cole, S. T. (2022). Decadal observations of internal wave energy, shear, and mixing in the western Arctic Ocean. *Journal of Geophysical Research: Oceans*, *127*(5), e2021JC018056. https://doi.org/10.1029/2021JC018056

Fine, E. C., MacKinnon, J. A., Alford, M. H., & Mickett, J. B. (2018). Microstructure observations of turbulent heat fluxes in a warm-core Canada Basin eddy. *Journal of Physical Oceanography*, *48*(10), 2397–2418. https://doi.org/10.1175/Jpo-D-18-0028.1

Firing, E., Hummon, J. M., & Chereskin, T. K. (2012). Improving the quality and accessibility of current profile measurements in the Southern Ocean. *Oceanography*, *25*(3), 164–165. https://doi.org/10.5670/oceanog.2012.91

Fortin, W. F. J., Holbrook, W. S., & Schmitt, R. W. (2016). Mapping turbulent diffusivity associated with oceanic internal lee waves offshore Costa Rica. *Ocean Science*, *12*(2), 601–612. https://doi.org/10.5194/os-12-601-2016

Garrett, C., & Munk, W. (1975). Space-time scales of internal waves: A progress report. *Journal of Geophysical Research*, *80*(3), 291–297. https://doi.org/10.1029/JC080i003p00291

Gong, Y., Song, H., Zhao, Z., Guan, Y., Zhang, K., Kuang, Y., & Fan, W. (2021). Enhanced diapycnal mixing with polarity-reversing internal solitary waves revealed by seismic reflection data. *Nonlinear Processes in Geophysics*, *28*(3), 445–465. https://doi.org/10.5194/npg-28-445-2021

Gregg, M. C. (1989). Scaling turbulent dissipation in the thermocline. *Journal of Geophysical Research*, *94*(C7), 9686–9698. https://doi.org/10.1029/JC094iC07p09686

Gregg, M. C., Sanford, T. B., & Winkel, D. P. (2003). Reduced mixing from the breaking of internal waves in equatorial waters. *Nature*, *422*(6931), 513–515. https://doi.org/10.1038/nature01507

Gula, J., Blacic, T. M., & Todd, R. E. (2019). Submesoscale coherent vortices in the Gulf Stream. *Geophysical Research Letters*, *46*(5), 2704–2714. https://doi.org/10.1029/2019gl081919

Gunn, K. L., Dickinson, A., White, N. J., & Caulfield, C.-C. P. (2021). Vertical mixing and heat fluxes conditioned by a seismically imaged oceanic front. *Frontiers in Marine Science*, *8*. https://doi.org/10.3389/fmars.2021.697179

Hansen, J., Russell, G., Lacis, A., Fung, I., Rind, D., & Stone, P. (1985). Climate response times: Dependence on climate sensitivity and ocean mixing. *Science*, *229*(4716), 857–859. https://doi.org/10.1126/science.229.4716.857

Holbrook, W. S., & Fer, I. (2005). Ocean internal wave spectra inferred from seismic reflection transects. *Geophysical Research Letters*, *32*(15), L15604. https://doi.org/10.1029/2005GL023733

Holbrook, W. S., Fer, I., Schmitt, R. W., Lizarralde, D., Klymak, J. M., Helfrich, L. C., & Kubichek, R. (2013). Estimating oceanic turbulence dissipation from seismic images. *Journal of Atmospheric and Oceanic Technology*, *30*(8), 1767–1788. https://doi.org/10.1175/Jtech-D-12-00140.1

Holbrook, W. S., Paramo, P., Pearse, S., & Schmitt, R. W. (2003). Thermohaline fine structure in an oceanographic front from seismic reflection profiling. *Science*, *301*(5634), 821–824. https://doi.org/10.1126/science.1085116

Hua, B. L., Ménesguen, C., Le Gentil, S., Schopp, R., Marsset, B., & Aiki, H. (2013). Layering and turbulence surrounding an anticyclonic oceanic vortex: In situ observations and quasi-geostrophic numerical simulations. *Journal of Fluid Mechanics*, *731*, 418–442. https://doi.org/10.1017/jfm.2013.369

Kawaguchi, Y., Itoh, M., & Nishino, S. (2012). Detailed survey of a large baroclinic eddy with extremely high temperatures in the Western Canada Basin. *Deep-Sea Research Part I Oceanographic Research Papers*, *66*, 90–102. https://doi.org/10.1016/j.dsr.2012.04.006

Klymak, J. M., & Moum, J. N. (2007a). Oceanic isopycnal slope spectra. Part I: Internal waves. *Journal of Physical Oceanography*, *37*(5), 1215–1231. https://doi.org/10.1175/jpo3073.1

Klymak, J. M., & Moum, J. N. (2007b). Oceanic isopycnal slope spectra. Part II: Turbulence. *Journal of Physical Oceanography*, *37*(5), 1232–1245. https://doi.org/10.1175/jpo3074.1

Krahmann, G., Papenberg, C., Brandt, P., & Vogt, M. (2009). Evaluation of seismic reflector slopes with a Yoyo-CTD. *Geophysical Research Letters*, *36*, L00D02. https://doi.org/10.1029/2009gl038964

Kubryakov, A. A., Kozlov, I. E., & Manucharyan, G. E. (2021). Large mesoscale eddies in the Western Arctic Ocean from satellite altimetry measurements. *Journal of Geophysical Research: Oceans*, *126*(5), e2020JC016670. https://doi.org/10.1029/2020JC016670

Kunze, E., Firing, E., Hummon, J. M., Chereskin, T. K., & Thurnherr, A. M. (2006). Global abyssal mixing inferred from lowered ADCP shear and CTD strain profiles. *Journal of Physical Oceanography*, *36*(8), 1553–1576. https://doi.org/10.1175/Jpo2926.1

Lin, L., He, H., Cao, Y., Li, T., Liu, Y., & Wang, M. (2022). Oceanic vertical mixing of the lower halocline water at the Chukchi Borderland and Mendeleyev Ridge. *Acta Oceanologica Sinica*, *40*(11), 39–49. https://doi.org/10.1007/s13131-021-1825-z

Manley, T. O., & Hunkins, K. (1985). Mesoscale eddies of the Arctic Ocean. *Journal of Geophysical Research*, *90*(C3), 4911–4930. https://doi.org/10.1029/JC090iC03p04911

Mashayek, A., Salehipour, H., Bouffard, D., Caulfield, C. P., Ferrari, R., Nikurashin, M., et al. (2017). Efficiency of turbulent mixing in the abyssal ocean circulation. *Geophysical Research Letters*, *44*(12), 6296–6306. https://doi.org/10.1002/2016GL072452

Ménesguen, C., Hua, B. L., Carton, X., Klingelhoefer, F., Schnürle, P., & Reichert, C. (2012). Arms winding around a meddy seen in seismic reflection data close to the Morocco coastline. *Geophysical Research Letters*, *39*(5), L05604. https://doi.org/10.1029/2011gl050798

Muench, R. D., Gunn, J. T., Whitledge, T. E., Schlosser, P., & Smethie, W. (2000). An Arctic Ocean cold core eddy. *Journal of Geophysical Research*, *105*(C10), 23997–24006. https://doi.org/10.1029/2000jc000212

Munk, W., & Wunsch, C. (1998). Abyssal recipes II: Energetics of tidal and wind mixing. *Deep-Sea Research Part I Oceanographic Research Papers*, *45*(12), 1977–2010. https://doi.org/10.1016/S0967-0637(98)00070-3

Nghiem, S. V., Rigor, I. G., Perovich, D. K., Clemente-Colón, P., Weatherly, J. W., & Neumann, G. (2007). Rapid reduction of Arctic perennial sea ice. *Geophysical Research Letters*, *34*(19), L19504. https://doi.org/10.1029/2007gl031138

21699291, 2023, 10, Downloaded from https://agupubs.onlinelibrary.wiley.com/doi/10.1029/2023JC019964 by Tongji University, Wiley Online Library on [05/09/2024]. See the Terms and Conditions (https://onlinelibrary.wiley.com/terms-and-conditions) on Wiley Online Library for rules of use; OA articles are governed by the applicable Creative Commons License

Nurser, A. J. G., & Bacon, S. (2014). The Rossby radius in the Arctic Ocean. *Ocean Science*, *10*(6), 967–975. https://doi.org/10.5194/os-10-967-2014

Osborn, T. R. (1980). Estimates of the local rate of vertical diffusion from dissipation measurements. *Journal of Physical Oceanography*, *10*(1), 83–89. https://doi.org/10.1175/1520-0485(1980)010<0083:EOTLRO>2.0.CO;2

Qi, Y., Shang, C., Mao, H., Qiu, C., Liang, C., Yu, L., et al. (2020). Spatial structure of turbulent mixing of an anticyclonic mesoscale eddy in the northern South China Sea. *Acta Oceanologica Sinica*, *39*(11), 69–81. https://doi.org/10.1007/s13131-020-1676-z

Rainville, L., & Winsor, P. (2008). Mixing across the Arctic Ocean: Microstructure observations during the Beringia 2005 expedition. *Geophysical Research Letters*, *35*(8), L08606. https://doi.org/10.1029/2008gl033532

Rippeth, T., & Fine, E. (2022). Turbulent mixing in a changing Arctic Ocean. *Oceanography*, *35*(3–4), 66–75. https://doi.org/10.5670/oceanog.2022.103

Ruddick, B., Song, H. B., Dong, C. Z., & Pinheiro, L. (2009). Water column seismic images as maps of temperature gradient. *Oceanography*, *22*(1), 192–205. https://doi.org/10.5670/oceanog.2009.19

Sallares, V., Biescas, B., Buffett, G., Carbonell, R., Danobeitia, J. J., & Pelegri, J. L. (2009). Relative contribution of temperature and salinity to ocean acoustic reflectivity. *Geophysical Research Letters*, *36*(24), L00D06. https://doi.org/10.1029/2009GL040187

Schulz, K., Kadko, D., Mohrholz, V., Stephens, M., & Fer, I. (2023). Winter vertical diffusion rates in the Arctic Ocean, estimated from ^{7}Be measurements and dissipation rate profiles. *Journal of Geophysical Research: Oceans*, *128*(2), e2022JC019197. https://doi.org/10.1029/2022JC019197

Shaw, W. J., & Stanton, T. P. (2014). Vertical diffusivity of the western Arctic Ocean halocline. *Journal of Geophysical Research: Oceans*, *119*(8), 5017–5038. https://doi.org/10.1002/2013JC009598

Sheen, K. L., White, N. J., & Hobbs, R. W. (2009). Estimating mixing rates from seismic images of oceanic structure. *Geophysical Research Letters*, *36*(24), L00D04. https://doi.org/10.1029/2009GL040106

Song, H. B., Pinheiro, L. M., Ruddick, B., & Teixeira, F. C. (2011). Meddy, spiral arms, and mixing mechanisms viewed by seismic imaging in the Tagus Abyssal Plain (SW Iberia). *Journal of Marine Research*, *69*(4–6), 827–842. https://doi.org/10.1357/002224011799849309

Spall, M. A., Pickart, R. S., Fratantoni, P. S., & Plueddemann, A. J. (2008). Western Arctic shelfbreak eddies: Formation and transport. *Journal of Physical Oceanography*, *38*(8), 1644–1668. https://doi.org/10.1175/2007JPO3829.1

Tang, Q., Gulick, S. P. S., Sun, J., Sun, L., & Jing, Z. (2020). Submesoscale features and turbulent mixing of an oblique anticyclonic eddy in the Gulf of Alaska investigated by marine seismic survey data. *Journal of Geophysical Research: Oceans*, *125*(1), e2019JC015393. https://doi.org/10.1029/2019jc015393

Tang, Q., Jing, Z., Li, J., & Sun, J. (2022). Enhanced diapycnal mixing in the deep ocean around the Island of Taiwan. *Journal of Geophysical Research: Oceans*, *127*(5), e2021JC018034. https://doi.org/10.1029/2021jc018034

Tang, Q., Jing, Z., Lin, J., & Sun, J. (2021). Diapycnal mixing in the subthermocline of the Mariana Ridge from high-resolution seismic images. *Journal of Physical Oceanography*, *51*(4), 1283–1300. https://doi.org/10.1175/JPO-D-200120.s1

Thorpe, S. A. (2007). *An introduction to ocean turbulence*. Cambridge University Press.

Timmermans, M. L., Toole, J., Proshutinsky, A., Krishfield, R., & Plueddemann, A. (2008). Eddies in the Canada Basin, Arctic Ocean, observed from ice-tethered profilers. *Journal of Physical Oceanography*, *38*(1), 133–145. https://doi.org/10.1175/2007JPO3782.1

Voet, G., Drake, H., & Cusack, J. (2022). Ocean mixing parameterizations in python. Version 0.1.1 [Software]. Github. https://github.com/modscripps/mixsea

Wang, Q. Y., Dong, C. M., Dong, J. H., Zhang, H., & Yang, J. S. (2022). Submesoscale processes-induced vertical heat transport modulated by oceanic mesoscale eddies. *Deep-Sea Research Part II Topical Studies in Oceanography*, *202*, 105138. https://doi.org/10.1016/j.dsr2.2022.105138

Wei, J., Gunn, K. L., & Reece, R. (2022). Mid-ocean ridge and storm enhanced mixing in the Central South Atlantic thermocline. *Frontiers in Marine Science*, *8*, 771973. https://doi.org/10.3389/fmars.2021.771973

Whalen, C. B., MacKinnon, J. A., & Talley, L. D. (2018). Large-scale impacts of the mesoscale environment on mixing from wind-driven internal waves. *Nature Geoscience*, *11*(11), 842–847. https://doi.org/10.1038/s41561-018-0213-6

Wunsch, C., & Ferrari, R. (2004). Vertical mixing, energy, and the general circulation of the oceans. *Annual Review of Fluid Mechanics*, *36*(1), 281–314. https://doi.org/10.1146/annurev.fluid.36.050802.122121

Xiao, W., & Meng, Z. (2022). Turbulent heat fluxes in a Mediterranean eddy quantified using seismic and hydrographic observations. *Journal of Marine Science and Engineering*, *10*(6), 720. https://doi.org/10.3390/jmse10060720

Yang, Q., Zhao, W., Liang, X., Dong, J., & Tian, J. (2017). Elevated mixing in the periphery of mesoscale eddies in the South China Sea. *Journal of Physical Oceanography*, *47*(4), 895–907. https://doi.org/10.1175/jpo-d-16-0256.1

Yang, S., Coakley, B., Frambach, A., & Hummon, J. (2023). ADCP data from the Chukchi Sea, Arctic Ocean, acquired during the R/V Marcus G. Langseth expedition MGL1112 (version 1) [Dataset]. Zenodo. https://doi.org/10.5281/zenodo.8228991

Yang, S., Song, H., Coakley, B., Zhang, K., & Fan, W. (2022). A mesoscale eddy with submesoscale spiral bands observed from seismic reflection sections in the Northwind Basin, Arctic Ocean. *Journal of Geophysical Research: Oceans*, *127*(3), e2021JC017984. https://doi.org/10.1029/2021JC017984

Yang, S., Song, H. B., Fan, W. H., & Wu, D. (2021). Submesoscale features of a cyclonic eddy in the Gulf of Papagayo, Central America. *Chinese Journal of Geophysics-Chinese Edition*, *64*(4), 1328–1340. https://doi.org/10.6038/cjg2021O0204

Yilmaz, O. (2001). Seismic Data Analysis: Processing, inversion, and interpretation of seismic data. *Society of Exploration Geophysicists*.

Zhang, K., Song, H., Coakley, B., Yang, S., & Fan, W. (2022). Investigating eddies from coincident seismic and hydrographic measurements in the Chukchi Borderlands, the western Arctic Ocean. *Journal of Geophysical Research: Oceans*, *127*(10), e2022JC018453. https://doi.org/10.1029/2022jc018453

Zhang, X., Dai, H., Zhao, J., & Yin, H. (2019). Generation mechanism of an observed submesoscale eddy in the Chukchi Sea. *Deep Sea Research Part I: Oceanographic Research Papers*, *148*, 80–87. https://doi.org/10.1016/j.dsr.2019.04.015

Zhang, Z., & Qiu, B. (2020). Surface chlorophyll enhancement in mesoscale eddies by submesoscale spiral bands. *Geophysical Research Letters*, *47*(14), e2020GL088820. https://doi.org/10.1029/2020GL088820

Zhao, M. N., & Timmermans, M. L. (2015). Vertical scales and dynamics of eddies in the Arctic Ocean's Canada Basin. *Journal of Geophysical Research: Oceans*, *120*(12), 8195–8209. https://doi.org/10.1002/2015JC011251

Zhao, M. N., Timmermans, M. L., Cole, S., Krishfield, R., Proshutinsky, A., & Toole, J. (2014). Characterizing the eddy field in the Arctic Ocean halocline. *Journal of Geophysical Research: Oceans*, *119*(12), 8800–8817. https://doi.org/10.1002/2014jc010488

Zhao, M. N., Timmermans, M. L., Cole, S., Krishfield, R., & Toole, J. (2016). Evolution of the eddy field in the Arctic Ocean's Canada Basin, 2005-2015. *Geophysical Research Letters*, *43*(15), 8106–8114. https://doi.org/10.1002/2016GL069671

Zhong, W., Guo, G., Zhao, J., Li, T., Wang, X., & Mu, L. (2018). Turbulent mixing above the Atlantic Water around the Chukchi Borderland in 2014. *Acta Oceanologica Sinica*, *37*(3), 31–41. https://doi.org/10.1007/s13131-018-1198-0

21699291, 2023, 10, Downloaded from https://agupubs.onlinelibrary.wiley.com/doi/10.1029/2023JC019964 by Tongji University, Wiley Online Library on [05/09/2024]. See the Terms and Conditions (https://onlinelibrary.wiley.com/terms-and-conditions) on Wiley Online Library for rules of use; OA articles are governed by the applicable Creative Commons License